Advances in Analytic Science 2024, 5(2), 2665.
https://doi.org/10.54517/aas.v5i2.2665

Article

TLS noise reduction in microwave kinetic inductance detectors using a parallel plate capacitor with a three-layer dielectric

Zahra Ehsani, Seyed Mohammad Hassan Javadzadeh*, Mahboobeh Baghi Hedeshi

Department of Electrical Engineering, Shahed University, Tehran 470, Iran
*** Corresponding author:** Seyed Mohammad Hassan Javadzadeh, smh.javadzadeh@shahed.ac.ir

CITATION

Ehsani Z, Javadzadeh SMH, Hedeshi MB. TLS noise reduction in microwave kinetic inductance detectors using a parallel plate capacitor with a three-layer dielectric. Advances in Analytic Science. 2024; 5(2): 2665. https://doi.org/10.54517/aas.v5i2.2665

ARTICLE INFO

Received: 2 April 2024
Accepted: 16 July 2024
Available online: 29 August 2024

Abstract: Over the past two decades, microwave kinetic inductance detectors (MKIDs) have gained exceptional importance in millimeter and sub-millimeter astronomy. MKIDs consist of thin strip resonators capable of detecting changes in the surface impedance of superconductor strips, which result from variations in resonance circuit properties. The principal noise in MKIDs comprises excess frequency noise and two-level system noise. In this paper, we propose a technique to mitigate the effect of two-level system (TLS) noise in MKIDs using a parallel plate capacitor with three layers of high ε dielectrics. To achieve this, we employ three layers of Al_2O_3, HfO_2, and TiO_2 with equal thickness between the capacitor plates. The experimental results demonstrate a nearly 30% reduction in TLS power spectral density.

Keywords: microwave detectors; MKIDs; noise; two level system; capacitor; resonator

1. Introduction

The Microwave Kinetic Inductance Detector (MKID) is a photon-counting detector based on superconductors, designed to measure the arrival time and energy of each photon [1]. It operates as a highly sensitive low-temperature detector, first introduced in the early 2000s with the inherent capability to be integrated into large arrays [2]. MKIDs possess a distinctive feature of natural multiplexed readout [3] and intrinsic energy resolution ranging from 75 eV to 43 eV at 5.9 keV for near-infrared photons [4]. They are applicable across the millimeter, sub-millimeter, and far-infrared photon range, as well as for near-infrared single photon-counting [5,6]. MKIDs operate on a pair-breaking detection mechanism, leveraging alterations in the kinetic inductance of a thin superconductor film. Absorbed photons with an energy of $hf > 2\Delta$ break apart Cooper pairs, resulting in an excess quasiparticle population. This excess increases the kinetic inductance of the film, thereby altering its complex impedance. These changes in inductance can be detected through variations in resonance frequency and quality factor [7]. MKIDs utilize frequency-domain multiplexing readout to simultaneously read out as many as 2000 pixels [8], allowing them to detect athermal phonons with high performance [9]. Consequently, they are suitable for constructing large sensor arrays [6], which find various applications, notably in astronomy and astrophysics, particularly for large-format X-ray, gamma-ray, and optical imaging detectors. Additionally, they can be developed for energy-resolving spectrophotometers and on-chip filter bank spectrometers [10,11]. The range spanning from radio to far-infrared wavelengths represent one of the most significant yet underdeveloped segments of the electromagnetic spectrum. This range encompasses a substantial portion of the Cosmic Microwave Background (CMB) energy, which is invaluable for studying the early universe [6]. The unique properties

of Microwave Kinetic Inductance Detectors (MKIDs) render them an ideal choice for ground-based CMB observations [12], as they facilitate natural frequency domain application and offer rapid time response [13]. Polarization-sensitive MKIDs are currently under investigation for the next generation BLAST instrument (BLAST-TNG), a balloon-borne sub-millimeter polarimeter developed to study magnetic fields in diffuse dust regions and molecular clouds [14]. In general, MKIDs present desirable features compared to other detector technologies, boasting simpler fabrication processes and the ability to be integrated into multiplexing kilo-pixel detector arrays with suitable readout techniques [15]. During initial studies, most researchers believed that the predominant noise in MKIDs stemmed from quasiparticle generation-recombination processes. However, experimental measurements have revealed significant excess frequency noise, indicating that intrinsic MKID noise originates from multiple sources, including generation-recombination noise, Two-Level-System (TLS) noise [16], and High Electron Mobility Transistor (HEMT) amplifier noise [17]. TLS noise arises from interactions with two-level systems in the dielectric material of the microwave resonator [7], leading to jitter in the resonance frequency, which can be quantified and explained by the fractional frequency noise power spectral density (STLS) [18].

2. Kinetic inductance

Superconductors exhibit a complex surface impedance due to the reactive energy exchange between the superconductor and the electromagnetic (EM) field. Equation (1) defines the surface impedance in a superconductor.

$$Z_s = R_s + i\omega L_s \tag{1}$$

The surface impedance consists of a surface resistance R_s, which accounts for losses at angular frequency ω resulting from the small fraction of electrons not in Cooper pairs, known as quasiparticles [6]. The surface inductance, $L_s = \mu\lambda$ is a function of the superconducting penetration depth λ. Both λ and L_s are intrinsic characteristics of the material. Thinner films, those thinner than λ, typically exhibit higher surface inductance [19]. The ratio of inductance to resistance in thin superconducting films at low temperatures is notably large. This phenomenon is attributed to the significant kinetic energy of electrons in the Cooper pair state, as they move without scattering in a superconductor. The Kinetic Inductance of a superconductor can be derived by equating the equivalent inductive energy with the kinetic energy of the charge carriers.

$$n(lwd)m_e v^2 = \frac{1}{2}L_k I^2 \tag{2}$$

In Equation (2), n represents the density of Cooper pairs. Parameters $l, w,$ and d respectively denote the length, width, and thickness, defining the volume of the conductor. $2m_e$ signifies the mass of a Cooper pair, ν represents their average velocity, L_k stands for the kinetic inductance, and $I = 2en(wd)v$ denotes the current, where $2e$ represents the charge of a Cooper pair. Hence, we can utilize Equation (3) to compute the kinetic inductance.

$$L_k = \frac{m}{2ne^2}\frac{l}{wd} \tag{3}$$

The magnitude of kinetic inductance exceeding the resistance of a superconductor relies on the density of Cooper pairs. Consequently, breaking Cooper pairs into quasiparticles induces a discernible alteration in the superconductor's inductance. It's crucial to note that the Cooper pair density exhibits a nonlinear response to significant variations in current or temperature; hence, by extension, the kinetic inductance also demonstrates nonlinearity [10]. Equation (4) provides the total inductance, L.

$$L = L_k + L_{geo} \tag{4}$$

Another critical parameter in Microwave Kinetic Inductance Detectors (MKIDs) is the factor α. This factor describes the ratio of the portion of the total inductance of the film attributed to the kinetic inductance. Equation (5) expresses this ratio.

$$\alpha = L_k/(L_k + L_{geo}) \tag{5}$$

Designing the inductive part to be narrow is crucial to achieve a large value of α, which is necessary for maximizing responsivity.

3. MKIDs and their operation procedure

The Microwave Kinetic Inductance Detector (MKID) operates on the principle of pair breaking in a superconducting material, wherein radiation is absorbed, leading to quasiparticle excitations within the superconductor [2,20].

When a photon with energy greater than the superconducting energy gap ($hv > 2\Delta$) is absorbed by the material, the photon detection process in an MKID initiates. This photon's energy can break one or more Cooper pairs, triggering a cascade of interacting quasiparticles and phonons, which rapidly cool down. This cascade results in an excess population of quasiparticles with energies slightly higher than the energy gap, along with sub-gap phonons in the superconductor. These quasiparticle excitations persist until two quasiparticles combine to form a Cooper pair, emitting a phonon in the process. The presence of excess quasiparticles in a superconductor film alters its surface impedance, analogous to an increase in temperature. Although changes in surface impedance may be subtle, employing a resonant circuit enables efficient measurement. Variations in the surface inductance L_s and resistance R_s influence the resonance width and frequency, respectively, resulting in phase and amplitude changes of a microwave signal transmitted through the circuit [6]. **Figure 1** illustrates the principle of operation of an MKID.

The change in phase per injected quasiparticle, $\frac{\mathrm{d}\theta}{\mathrm{d}N_{qp}}$, is described as the detector's responsivity. When using the Mattis-Bardeen theory to calculate the responsivity of an MKID, we conclude that for a given superconductor and resonant frequency of a resonator, the responsivity scaling law states:

$$\frac{\mathrm{d}\theta}{\mathrm{d}N_{qp}} \propto \frac{\alpha Q}{V} \tag{6}$$

This equation indicates that to develop resonators with higher responsivity, we require higher α and quality factor, and lower volume [6].

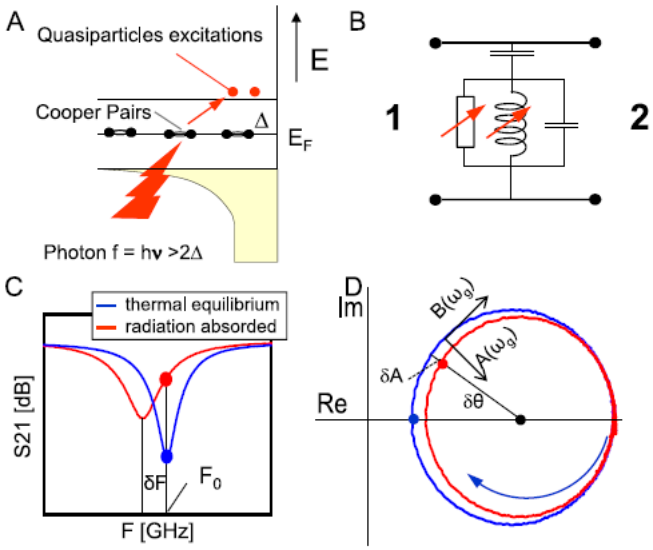

Figure 1. MKID principle of operation. **(A)** Photons break Cooper pairs, producing quasiparticles; **(B)** the resonance circuit can detect variations in Z_s after radiation absorption in the superconductor; **(C)** the transmission of one resonator between the two ports in (B) is measured. The blue line represents the equilibrium condition, changing to the red line when the detector absorbs a photon; **(D)** the data depicted in (C) is illustrated in the complex plane, indicating either a change in amplitude or phase. By setting the readout tone at F0, the amount of radiation absorbed by the detector can be measured. The direction of the arrow represents increasing frequency [20].

MKIDs feature two main types of structures: distributed MKIDs and lumped element MKIDs. The Quarter Wave resonator is the most common geometry for distributed devices. Its design incorporates a $\lambda/4$ transmission line, which is shorted at one end and capacitively coupled to another transmission line serving as the feed for the resonator. By setting the ratio of the center strip to gap width the same in the two sections, both parts of the transmission line are fabricated to have equal characteristic impedance Z_0, typically 50 ohms. **Figure 2** illustrates this quarter-wave resonator [21].

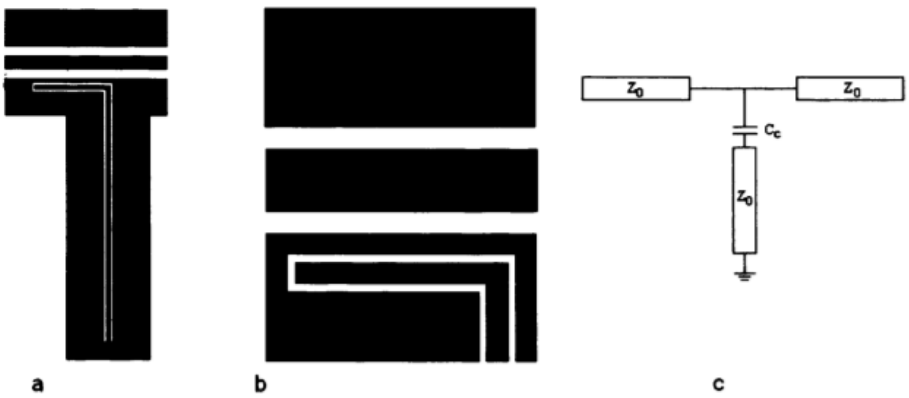

Figure 2. (a) Illustration of a CPW Quarter Wave resonator; **(b)** this figure shows a closer look at the capacitive coupling section; **(c)** the equivalent circuit model [21].

In distributed MKIDs, the distribution of current is not uniform along its length. It increases along the length of the line, being zero at the open end and reaching a maximum at the shorted end. This implies that the response of the distributed MKID is position-dependent on a pair-breaking event. Additionally, the performance of distributed MKIDs suffers limitations due to noise generated in the substrate of the structure [21].

One solution to the issue of optical coupling THz radiation in an MKID device is to develop a lumped element resonator, which, unlike the distributed version, does not exhibit any current variation along its length. In Lumped Element MKIDs (LEKIDs), the resonance circuit includes superconducting elements L and C, and changes in the density of Cooper pairs in the superconducting material shift the resonant frequency. Equation (7) gives the resonant frequency of this design.

$$\omega_0 = \frac{1}{\sqrt{LC}} \tag{7}$$

In the LEKID structure shown in **Figure 3**, the meander section serves as a lumped inductor comprising two parts: one attributed to the geometric inductance of the meander (L) and the other arising from the kinetic inductance due to the reactance of the Cooper pairs (L_k). Since the current distribution does not vary along the length of the meander, L_k remains constant. Therefore, alterations of L_k at any point on the meander will modify the total meander inductance, which is the sum of L and L_k. The interdigital section generates a series capacitor (C) with the meander, giving the whole structure a resonant frequency [22]:

$$\omega_0 = \frac{1}{\sqrt{(L + L_k)C}} \tag{8}$$

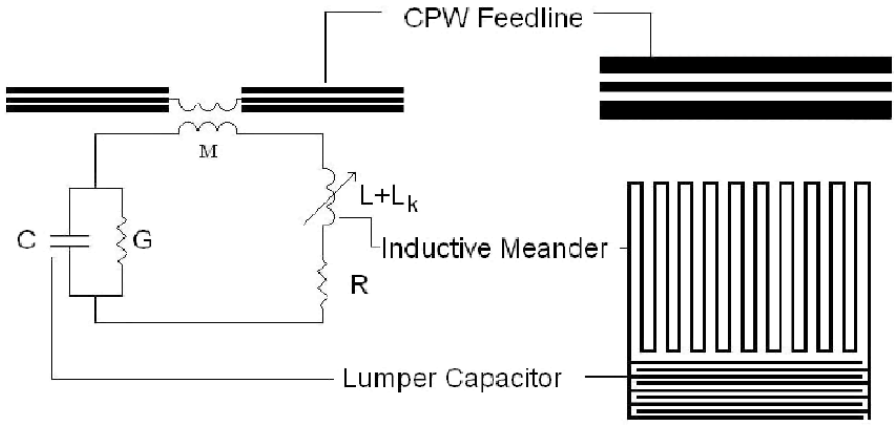

Figure 3. Schematic of a LEKID resonator (right) and its equivalent circuit (left) [21].

4. Noise in MKIDs

Noise in Microwave Kinetic Inductance Detectors (MKIDs) can originate from two different sources: fundamental noise, which arises from quasiparticles, and excess noise, which can be mitigated through design improvements.

Fundamental noise sources are attributed to quasiparticle fluctuations and photon

fluctuations, resulting in Generation-Recombination noise and photon noise, respectively [23].

The fluctuation in the kinetic inductance due to random thermal quasiparticles' generation and recombination in the superconductor constitutes a significant noise source. Since the number of thermal quasiparticles decreases exponentially as the temperature decreases, this noise source can be improved by operating at lower temperatures [6].

Photon noise occurs when the arrival rate of photons fluctuates randomly. Given that the radiation incident on the detector is essentially a stream of photons, the random arrival rate serves as an intrinsic noise source.

The sensitivity limit of a practical MKID is not solely determined by the generation-recombination noise but also by factors such as photon arrival rate, photon energy, and the time constant of the device. Equation (9) describes this sensitivity limit through the noise equivalent power, where η_{opt} represents the optical efficiency [20].

$$\mathrm{NEP}^2 = (\mathrm{NEP}_{G-R}^2 + \mathrm{NEP}_{\mathrm{photon}}^2)/\eta_{\mathrm{opt}} \tag{9}$$

The Fano Limit represents an intrinsic constraint on the energy resolution of optical, ultraviolet, or X-ray pulse counting detectors [6]. It serves as a fundamental limit for the energy resolution of all pair-breaking detectors [20]. This limit arises because the process of absorbing a photon and creating quasiparticles is inherently noisy [6].

In addition to intrinsic noise sources, MKIDs are also susceptible to excess noise. This excess noise source includes Two-Level System (TLS) noise and amplifier noise. The disordered structure of amorphous materials leads to the presence of two-level systems, where atoms or groups of atoms can transition between different configurations associated with two local potential energy minima through quantum tunneling over an energy barrier [6].

TLS causes the electric fields inside a microwave resonator to couple to the dipoles of the TLS. This coupling results in power being extracted from the resonator and converted to loss, thereby reducing the quality factor of the resonance. Moreover, the random nature of TLS tunneling events leads to fluctuations in the dielectric constant, which can induce excess frequency noise in superconducting resonators [18].

The MKID readout system can introduce additional noise, with the cryogenic Low-Noise Amplifier (LNA) in the setup being a dominant source, thus termed amplifier noise [24]. This amplifier noise, evident in the amplified, transmitted signal S_{21}, exhibits a white noise spectrum with constant power spectral density. Additionally, depending on the amplifier noise temperature T_N, it can manifest as phase and amplitude noise [23].

Increasing the input power can enhance the amplifier noise in MKIDs; however, it also reduces the quasiparticle recombination time and, consequently, the signal integration length [25]. Although higher readout power can lead to the creation of more quasiparticles, the efficiency is expected to be lower than that of photons with energies exceeding the gap energy. Therefore, a limitation to improving noise behavior through increased power lies in determining the extent to which power can be increased before worsening noise contributions due to nonlinear and saturation

behavior or excess quasiparticle creation. The creation of quasiparticles by increasing readout power partially offsets the improvements in frequency jitter and readout noise [26]. Thus, to minimize amplifier noise, the optimal readout power must be selected such that the rates of microwave and optical quasiparticle generation are nearly equal [27].

5. A historical overview of the noise study

The observation of excess noise and its impact on detector Noise Equivalent Power (NEP) began in 2002. Mazin et al. [28] introduced a new multiplexable readout technique for superconducting pair-breaking detectors. They proposed that microwave amplifier noise dominates the noise in phase measurement. Additionally, they suggested that the intrinsic noise of the detector is set by the random generation and recombination of quasiparticles by thermal phonons or the stochastic nature of the number of quasiparticles produced by a photon. Day et al. [2] conducted noise measurements on a 200 nm thick Aluminum on sapphire MKID. They observed that the NEP was limited by excess noise, although they did not fully understand the source of this excess noise at the time. Mazin [6] further investigated MKIDs as promising low-temperature detectors. He identified generation-recombination noise and Fano noise as theoretical noise sources for MKIDs and conducted several experiments to identify the substrate as the source of the excess noise. Baselmans et al. [29] constructed a high-*Q* Niobium MKID resonator for space-based instruments in sub-mm astronomy. The results from two batches of Niobium resonators fabricated on Si substrates demonstrated sensitivity below $NEP{\sim}10^{-20}\ \mathrm{W}/\sqrt{\mathrm{Hz}}$. Doyle et al. [30] elucidated that Niobium resonators could serve as low-noise detectors at modest cryogenic temperatures for terahertz radiation. At 1 K, the $\mathrm{NEP_{gr}}$ (Generation-Recombination Noise Equivalent Power) of a Niobium KID can be approximately $10^{-19}\ \mathrm{W}/\sqrt{\mathrm{Hz}}$, while an Aluminum KID must be cooled to around 130 mK to achieve the same $\mathrm{NEP_{gr}}$. Mazin et al. [31] developed position-sensitive detectors for X-ray spectra, comprising a tantalum photon absorber strip positioned between two aluminum MKIDs. They presented a review on the origin of noise in their resonators and confirmed that noise reduction could enhance the detector's energy resolution to nearly 12 eV. Gao et al. [16] investigated the power dependence of excess noise in MKIDs and observed that the power-law index is −1/2 and does not depend on the substrate and superconductor. However, the noise level heavily relies on the substrate. They theorized that fluorescence from TLSs in the dielectric material of the resonator could explain the excess noise. Barends et al. [32] measured the resonance frequency, quality factor, and phase noise of tantalum and niobium $\lambda/4$ resonators on silicon. They investigated non-monotonic frequency temperature dependence, observed a 1/f-like slope in the phase noise at low temperatures, and noted that the power dependence of the *Q* factor could be attributed to TLS in the Si dielectric. They theorized that the associated dielectric losses decrease as microwave field intensity increases. Baselmans et al. [33] obtained the NEP of 23 MKID resonators. Each resonator consisted of a 100 nm thick sputter-deposited aluminum layer on a high-impedance silicon substrate. They found that in most cases, utilizing the transmitted phase as the readout of the resonator resulted in a higher NEP compared to using the signal amplitude as the

readout. Additionally, they achieved a sensitivity of a NEP $= 10^{-18}\ \mathrm{W}/\sqrt{\mathrm{Hz}}$. For a high-quality factor resonator with a flat frequency spectrum. Gao [17], Kumar et al. [34] and Gao et al. [35] provided explanations for the power, temperature, and geometry dependence of excess frequency noise in MKIDs. They also proposed a semi-empirical model for TLS noise, which can be used to derive an equation for the TLS power spectrum. This model will be further discussed in the subsequent section. Noroozian et al. [36] utilized Gao's semi-empirical model to mitigate TLS noise in an MKID by implementing an interdigital capacitor. This approach resulted in an improvement in NEP by approximately a factor of $\sqrt{29}$. Czakon et al. [37] discussed the readout conditions of resonators in the Multiwavelength Sub-millimeter Inductance Camera (MUSIC) prototype under slightly nonlinear conditions. MUSIC employs MKIDs as their detecting elements. In their study, they successfully tripled the signal size and reduced the NEP by a factor of 10. Yates et al. [38] developed an innovative MKID array coupled to a lens-antenna fabricated from NbTiN and Al, capable of handling loading powers above 100 fW with high optical efficiency, achieving photon noise-limited detection. This advancement is valuable for the construction of very large MKID-based cameras for sub-mm astronomy. Shirokoff et al. [39] presented the design of KIDs utilized in SuperSpec, an ultra-compact spectrometer-on-a-chip for mm and sub-mm range astronomy. To mitigate the TLS contribution, they incorporated IDCs positioned on a crystalline *Si* substrate and operated at a readout frequency of a few hundred megahertz. Janssen et al. [40] introduced antenna-coupled hybrid NbTiNAl MKIDs designed for ground-based sub-mm astronomy. This MKID aims to simultaneously reduce TLS noise and increase phase response. They utilized NbTiN, which exhibits 10 dB lower TLS noise compared to conventional superconductors like Al. Lowitz et al. [41] and Araujo et al. [42] successfully reduced TLS noise in MKIDs by lowering the readout frequency. Ji [43] proposed the use of parallel plate capacitors to mitigate TLS noise in MKID resonators. This approach ensured an absorption efficiency of millimeter-wave power exceeding 80% and achieved a NEP close to background-limited performance. McCarrick et al. [44] and Johnson et al. [45] minimized the impact of TLS noise in their polarization-sensitive MKIDs by widening capacitor gaps. Bueno et al. [46] presented a background-limited broadband Kinetic Inductance Detector coupled to an antenna covering the frequency range from 1.4 to 2.8 THz. They reduced TLS noise in their device by adjusting the width of the gaps in the CPW design. Zobrist et al. [19] focused on reducing the impact of TLS and enhancing readout power in MKIDs by employing disk resonators. Beldi et al. [47] designed LEKIDs using parallel-plate capacitors to cover the optical and near-infrared spectrum. They highlighted that parallel-plate capacitors are ideal for reducing TLS noise due to the high electric field inside the capacitor. Hornsby et al. [48] compared LEKIDs with various coatings of SiNx to investigate their influence on resonant frequency, temperature dependence, and TLS noise. They discovered that separating the capacitive elements from the inductive components can mitigate additional TLS losses. Hailey-Dunsheath et al. [49] enhanced KID sensitivity to NEP $= 3 \times 10^{-19}\ \mathrm{W}/\sqrt{\mathrm{Hz}}$ by constructing antenna-coupled CPW resonators. These resonators were utilized for building large arrays for The Origins Space Telescope. Sueno et al. [50] studied methods for TLS noise

reduction in MKIDs using Nb film on Si substrates and hybrid-type MKIDs combining Al and Nb films. They succeeded in reducing TLS noise in the MKID by 5.5 dB. Hood et al. [51] developed a device for characterizing low-loss microstrips at 150 GHz for measurements of the millimeter-wavelength sky. They positioned MKIDs directly onto the microstrip dielectric for power measurement and reduced TLS noise in their MKID by removing the SiO_2 stop layer, which significantly impacted detector noise. Pan et al. [52] conducted a study investigating the impact of various modifications to the lumped-element inductor and interdigitated capacitor geometry of a series of MKIDs on noise performance in the millimeter-wave spectrum. They identified contributions from TLS noise in the dielectric layer, generation-recombination noise intrinsic to the superconducting thin-film, and system white noise from each detector noise power spectrum. The researchers characterized how these noise components depend on detector geometry, material properties, and measurement conditions such as driving power and temperature.

6. Methodology

In this paper, our objective is to mitigate the TLS noise in a lumped-element Microwave Kinetic Inductance Detector (LEKID) employing a parallel plate capacitor (**Figure 4**). We leverage Gao's semi-empirical model [17] to characterize the power spectrum of TLS noise, as described by Equation (10).

$$S_{\mathrm{TLS}} = \kappa(\nu, f_r, T)\frac{\int_{V_{TLS}}|E(r)|^3 d^3r}{4(\int_V|\varepsilon E(r)|^2 d^3r)^2} \tag{10}$$

The exponent 3 of the field ($|E(r)|^3$) suggests that TLS is most detrimental in the vicinity near the capacitive end (open-circuit) of the resonator. Here, ε represents the dielectric constant, V denotes the total volume of the resonator, and V_{TLS} indicates the volume containing TLS. The noise spectral density coefficient $\kappa(\nu, f_r, T)$ encapsulates the noise spectral shape, resonant frequency, and temperature dependence. Presently, there exists no definitive equation delineating how κ varies with frequency and temperature. However, it is understood that κ exhibits dependencies on frequency, power, temperature, and geometry.

$$S_{TLS} \propto f^{-2}P_{Readout}^{-\frac{1}{2}}T^{-2}s_r^{-1.6}\frac{\int_{V_{TLS}}|E(r)|^3 d^3r}{4(\int_V|\varepsilon E(r)|^2 d^3r)^2} \tag{11}$$

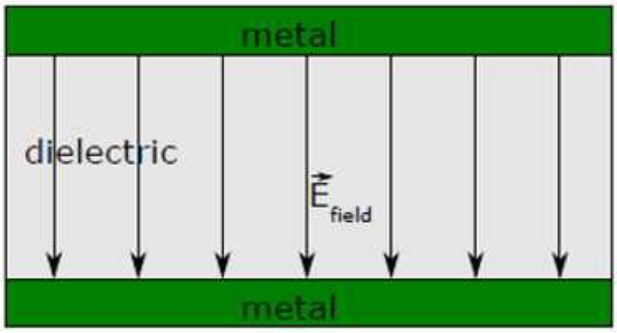

Figure 4. The electric field inside a parallel plate capacitor.

For a parallel plate capacitor $V_{\mathrm{TLS}} = V$ so, Equation (9) can be simplified as

$$S_{\mathrm{TLS}} \propto \frac{E^3 V}{4\varepsilon^2 E^4 V^2} \rightarrow S_{TLS} \propto \frac{1}{\varepsilon^2 EV} \tag{12}$$

Equation (12) delineates three fundamental approaches to diminish TLS noise: employing a material with a high dielectric constant (ε), augmenting the volume of the capacitor, or elevating the electric field within the capacitor, which entails operating the MKID at higher power. However, escalating the power in the resonator poses the risk of amplifying the current density, potentially leading to nonlinearity in resonance performance. Consequently, we opted to incorporate a multilayer dielectric within the capacitor (**Figure 5**). By doing so, we concurrently enhance both the effective dielectric constant and the volume.

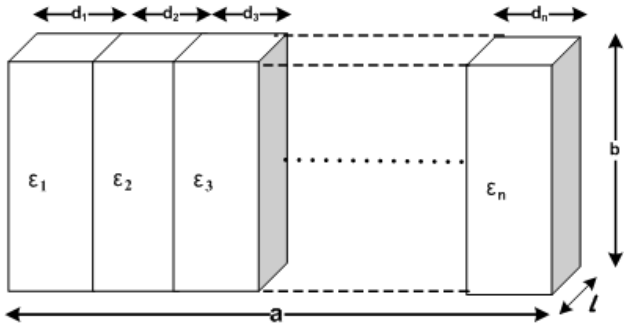

Figure 5. A multilayer dielectric.

For a multilayer dielectric parallel plate capacitor the effective ε is given by

$$\varepsilon_{eff} = \frac{\varepsilon_1 v_1 + \varepsilon_2 v_2 + \varepsilon_3 v_3 + \cdots + \varepsilon_n v_n}{v_1 + v_2 + v_3 + \cdots + v_n} \tag{13}$$

ε_i and v_i are the dielectric constant and volume of each layer, respectively. When the volume of each layer is equal

$$\varepsilon_{eff} = \frac{(\varepsilon_1 + \varepsilon_2 + \varepsilon_3 + \cdots + \varepsilon_n)v}{nv} = \frac{\sum_{i=1}^{n} \varepsilon_i}{n} \tag{14}$$

We employed a three-layer capacitor with dielectrics horizontally positioned on top of each other (**Figure 6**). This design is equivalent to three separate capacitors with one layer of dielectric connected in series.

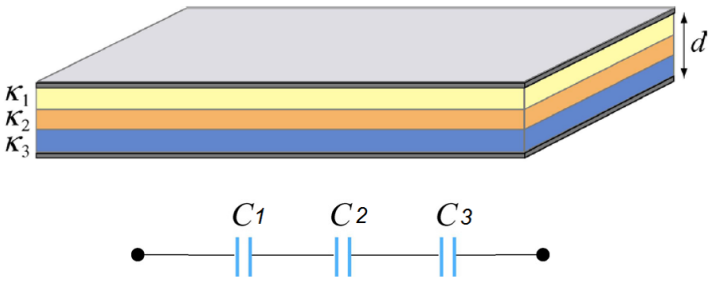

Figure 6. A three-layer dielectric capacitor and its equivalent circuit.

For a parallel plate capacitor design, Equation (9) will be

$$S_{TLS} = \kappa(\nu, f_r, T) \frac{4 \int_{A_{TLS}} \rho(x,y)^3 \, dx \, dy}{3\pi C^2 V_0 l} \quad (15)$$

where C is the capacitance of the open (capacitive) end of the resonator, l indicates the resonator length, V_0 is the voltage at the capacitive end (normalized to V_0 = 1 V), and ρ (x, y) is the electric field distribution in the cross-sectional plane.

Considering we lack the means to calculate the exact value of $\kappa(\nu, f_r, T)$, we cannot determine an exact value for S. However, for the purpose of this paper, which is not to determine the noise level but to compare it, we can simplify Equation (15) in a similar manner to Equation (12).

$$S_{\mathrm{TLS}} \propto \frac{\rho(x,y)^3 A}{C^2 V_0 l} \quad (16)$$

This approach allows us to obtain an approximate value for the TLS noise in each dielectric layer. Consequently, if we assume that the TLS noise of these layers is additive, we can derive an approximate value for TLS noise in our three-layer structure.

7. Simulation and results

We utilized CST for simulating a LEKID (**Figure 7**), comprising a parallel plate capacitor and a meandered inductor, inductively coupled to a 50 Ω niobium CPW feed line. The sensitivity of MKID depends on the critical temperature in reverse. Therefore, sub-stoichiometric TiN with a critical temperature below 1 K was chosen as the material for the resonance circuit. However, one limitation of this material is its sensitivity to the proportion of Ti and N [15]. To achieve optimal performance, we cooled the device to Tc/8 (where Tc ~4.6 K). Our TiN film is 52 nm thick, yielding a sheet kinetic inductance of L_k~8 pH per square. The gap between strips and the width of each strip are 0.5 μm and 2.5 μm respectively. The inductive meander is connected to the parallel plate capacitor, fabricated from two 40 × 100 μm TiN plates. A thin 25 nm Al_2O_3 layer with a dielectric constant of approximately εr10 is placed between the plates, and the resonator size is 112 × 85 μm.

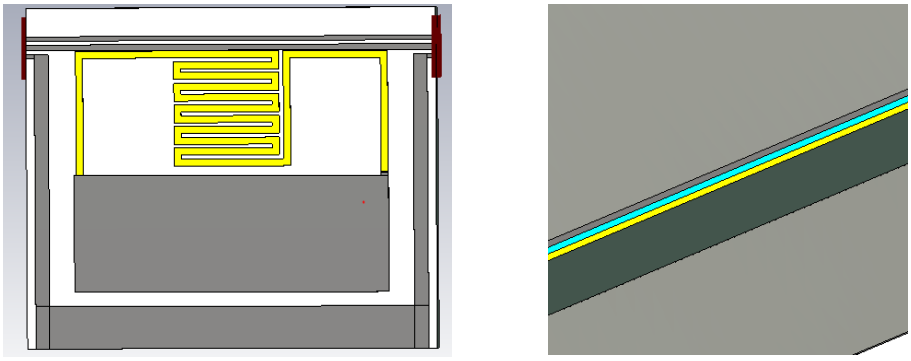

(a) **(b)**

Figure 7. (a) Our simulated LEKID design; **(b)** the capacitor cross-section.

The frequency response of the resonator exhibits a resonance at 0.9596 GHz (**Figure 8**).

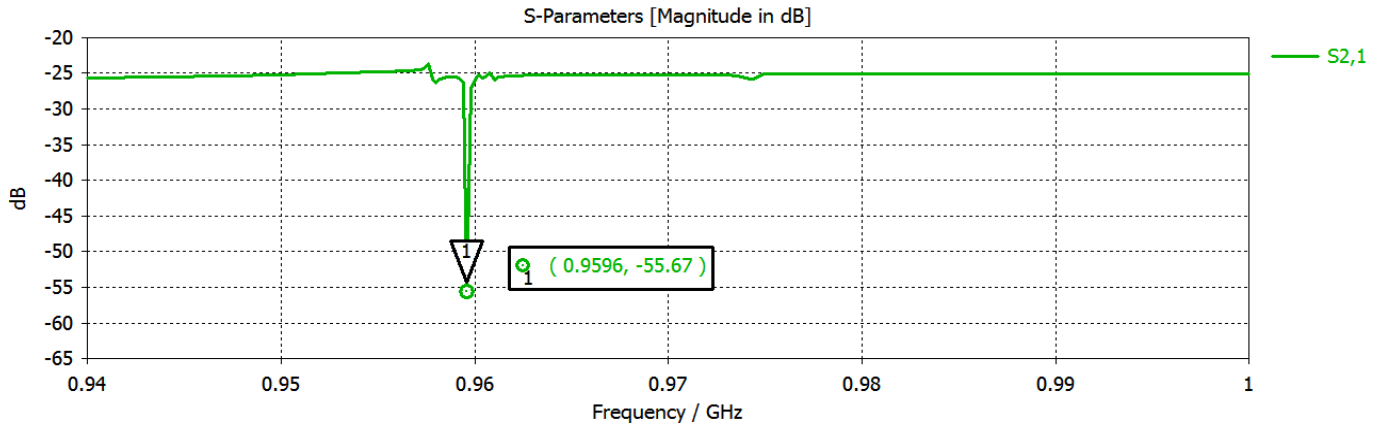

Figure 8. LEKID frequency response.

We calculated an approximate S_{TLS} value based on the equations outlined in the methodology section (**Table 1**). It's important to note that the values derived in this section are not exact representations of the TLS spectral density but rather approximations intended for comparison purposes only (**Figure 9**).

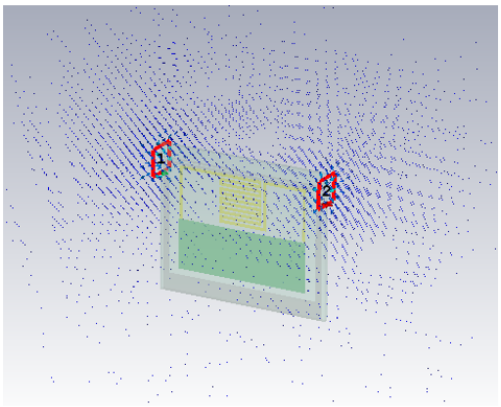

x [um]	y [um]	z [um]	ExRe [V/m]	ExIm [V/m]	EyRe [V/m]	EyIm [V/m]	EzRe [V/m]	EzIm [V/m]
-99.1125	-205.583	-106.232	-187.262	-148.448	141.379	-130.235	-50.1507	-134.437
-85.5835	-205.583	-106.232	-203.238	-94.0619	295.303	-170.506	151.727	-119.166
-72.0545	-205.583	-106.232	-109.875	-54.0818	293.31	-190.541	191.644	-103.68
-58.5255	-205.583	-106.232	-35.9058	-26.4402	314.665	-198.076	239.683	-86.8318
-44.9965	-205.583	-106.232	18.6688	-11.137	359.367	-193.11	295.845	-68.6207
-31.4675	-205.583	-106.232	53.8491	-8.17212	427.417	-175.643	360.13	-49.0468
-17.9385	-205.583	-106.232	69.6352	-17.5457	518.816	-145.675	432.54	-28.1104
-4.4095	-205.583	-106.232	66.0271	-39.2577	633.562	-103.206	513.073	-5.81125
9.1195	-205.583	-106.232	43.0248	-73.3081	771.656	-48.2371	601.73	17.8506
22.6485	-205.583	-106.232	-249.959	-93.6994	570.328	-47.9196	484.967	40.1083
36.1775	-205.583	-106.232	-251.099	-75.7184	302.842	-44.5031	248.052	34.0266
49.7065	-205.583	-106.232	-221.002	-59.8775	89.6859	-39.6889	64.4275	32.4571
63.2355	-205.583	-106.232	-159.666	-46.1766	-69.1395	-33.477	-65.9063	35.3993
76.7645	-205.583	-106.232	-67.0935	-34.6158	-173.633	-25.8672	-142.948	42.854
90.2935	-205.583	-106.232	56.7174	-25.195	-223.795	-16.8598	-166.699	54.8206
103.822	-205.583	-106.232	211.766	-17.9143	-219.627	-6.45469	-137.159	71.2993
117.351	-205.583	-106.232	398.052	-12.7736	-161.127	5.34828	-54.3281	92.2902
130.88	-205.583	-106.232	366.749	-32.4535	-386.31	46.8196	-131.468	96.2984
144.409	-205.583	-106.232	169.822	-51.0108	-466.687	-5.62966	-171.747	63.6982
157.938	-205.583	-106.232	25.8561	-57.8223	-530.591	-46.5034	-214.313	33.4124
171.467	-205.583	-106.232	-65.1483	-52.8883	-578.021	-75.8016	-259.167	5.44038
184.996	-205.583	-106.232	-103.192	-36.2087	-608.977	-93.5243	-306.308	-20.2172
198.525	-205.583	-106.232	-88.2736	-7.78337	-623.459	-99.6714	-355.738	-43.5607
212.054	-205.583	-106.232	-20.3942	32.3875	-621.468	-94.2431	-407.455	-64.5901
225.584	-205.583	-106.232	100.446	84.304	-603.003	-77.2391	-461.46	-83.3051

Figure 9. LEKID electric field data.

Table 1. Results of LEKID with one Al_2O_3 layer dielectric between capacitor plates.

	ε	C	R	E	S_{TLS}
One layer dielectric	10	1.6	$6.2500 \times 10^{+14}$	1×10^{-9}	$1 \times 10^{+23}$

Table 2. High ε varepsilon dielectrics and their permittivity.

Material	**Electric permittivity**
Al_2O_3	10
HfO_2	25
SiO_2	4
TiO_2	50
CeO_2	20
Ta_2O_5	25

To enhance this design, we opted to incorporate a multilayer dielectric between the capacitor plates. This approach serves to elevate both the dielectric constant and

the capacitor volume. **Table 2** presents several dielectric options with high dielectric constants. While we initially utilized Al_2O_3. For the single-layer dielectric, for our upgraded design, we elected to incorporate two additional layers of HfO_2 and TiO_2. These materials boast high ε and have seen increasing use in microstrip circuits in recent years. By employing this three-layer dielectric capacitor, we achieve a higher effective permittivity compared to using Al_2O_3 alone. Notably, all three layers are of equal thickness, matching that of the single-layer design (25 nm).

The resonance frequency of the LC resonator is given by $f_r = 1/2\pi\sqrt{CL}$. While the inductive part of our resonator remains unchanged, the capacitor has been enlarged, resulting in a greater capacitance (**Figure 10**). Consequently, we observe a shift in the resonance frequency within the frequency response of the new structure, along with an augmented quality factor, signifying an enhancement in performance (**Figure 11**).

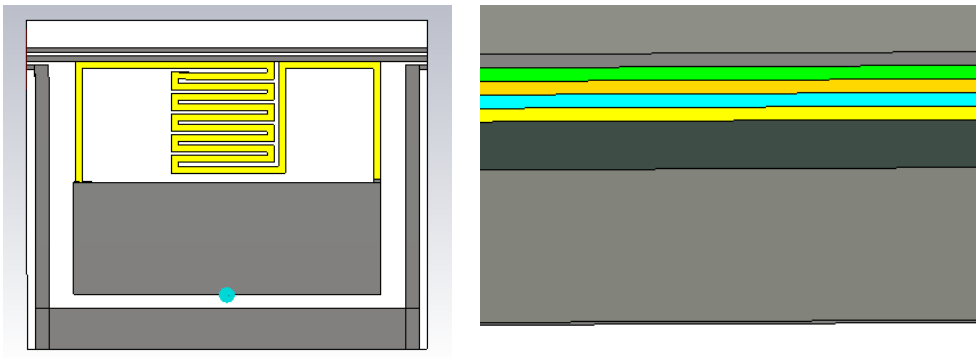

(a) **(b)**

Figure 10. (a) Our simulated three layers LEKID design; **(b)** the capacitor cross-section.

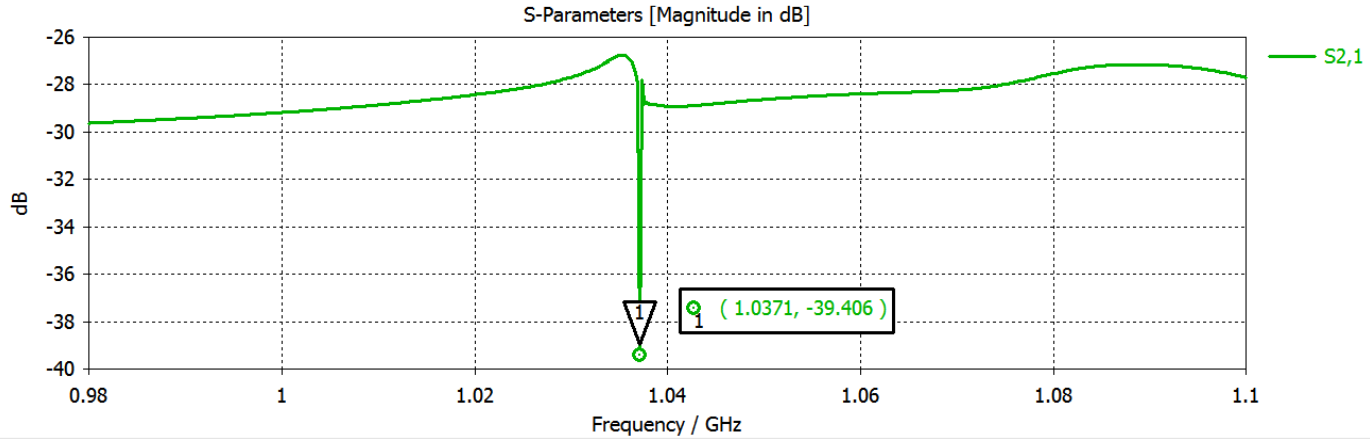

Figure 11. Three layers LEKID frequency response.

Considering the dielectric thickness was significantly small relative to the dimensions of the rest of the resonator, the electric field depicted in **Figures 9** and **12** did not provide us with the electric field between the capacitor plates. Consequently, we decided to derive electric field values from theoretical equations rather than relying on software.

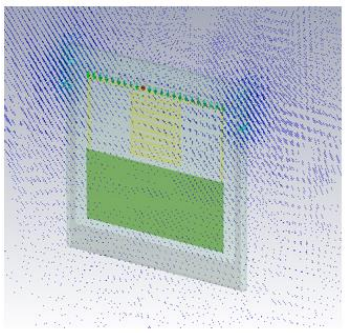

x [um]	y [um]	z [um]	ExRe [V/m]	ExIm [V/m]	EyRe [V/m]	EyIm [V/m]	EzRe [V/m]	EzIm [V/m]
144.409	-192.054	-106.232	197.201	-3.91292	-641.242	38.1171	-713.051	337.755
157.938	-192.054	-106.232	-2.36771	-12.1458	-708.005	9.7361	-821.319	310.069
171.467	-192.054	-106.232	-148.975	-8.63302	-758.296	-7.06928	-931.876	284.698
184.996	-192.054	-106.232	-242.621	6.62535	-792.112	-12.2993	-1044.72	261.641
198.525	-192.054	-106.232	-283.306	33.6293	-809.454	-5.95362	-1159.85	240.898
212.054	-192.054	-106.232	-271.03	72.379	-810.323	11.9675	-1277.27	222.469
225.584	-192.054	-106.232	-205.792	122.874	-794.718	41.4642	-1396.98	206.354
239.113	-192.054	-106.232	547.084	38.0991	-315.033	-61.954	-666.406	-31.5087
-99.1125	-178.525	-106.232	-107.694	-49.586	538.303	-114.429	376.894	-79.9858
-85.5835	-178.525	-106.232	-61.6036	-35.0784	793.382	-95.7196	2514.34	-168.564
-72.0545	-178.525	-106.232	-511.829	19.0171	1209.27	-92.8753	3693.74	-139.281
-58.5255	-178.525	-106.232	-337.755	25.0496	1090.22	-112.617	3595.95	-94.9319
-44.9965	-178.525	-106.232	-183.076	18.7437	994.508	-119.857	3506.3	-49.2201
-31.4675	-178.525	-106.232	-47.7905	0.0994339	922.149	-114.597	3424.76	-2.1456
-17.9385	-178.525	-106.232	68.1005	-30.8833	873.138	-96.8362	3351.35	46.2915
-4.4095	-178.525	-106.232	164.597	-74.2044	847.475	-66.5744	3286.06	96.0912
9.1195	-178.525	-106.232	-5.87402	-120.751	685.248	-82.6025	3070.84	150.173
22.6485	-178.525	-106.232	-178.145	-78.9378	457.016	-47.8674	2549.68	176.564

Figure 12. Three layers LEKID electric field data.

Given that the conductivity of the dielectric layers is non-zero, we can conceptualize each layer of dielectric within our capacitor as a simple resistor (**Table 3**). Consequently, we represent the equivalent circuit of our capacitor as depicted in **Figure 13**.

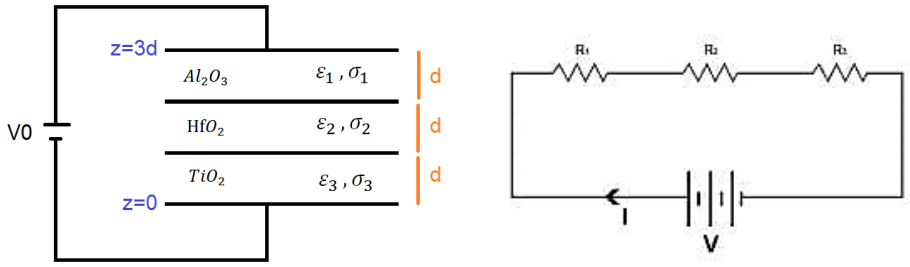

(a) **(b)**

Figure 13. (a) Schematic of our proposed three-layer capacitor; **(b)** the equivalent circuit considering $\sigma \neq 0$.

In the equivalent circuit illustrated in **Figure 13**, the resistance of each resistor can be calculated using Equations (17)–(19), and subsequently utilized to determine the electric field inside each dielectric layer.

$$R_1 = \frac{d}{\sigma_1 S} \tag{17}$$

$$R_2 = \frac{d}{\sigma_2 S} \tag{18}$$

$$R_3 = \frac{d}{\sigma_3 S} \tag{19}$$

$$I = \frac{V_0}{R_1 + R_2 + R_3} = V_0 / \left(\frac{d}{\sigma_1 S} + \frac{d}{\sigma_2 S} + \frac{d}{\sigma_3 S}\right) \tag{20}$$

$$I = \frac{V_0 S}{d}(\sigma_1 + \sigma_2 + \sigma_3) \tag{21}$$

$$J = \frac{I}{S} \tag{22}$$

$$J = \frac{V_0}{d}(\sigma_1 + \sigma_2 + \sigma_3) \tag{23}$$

$$J = \sigma E \tag{24}$$

Table 3. The conductivity of our chosen dielectrics.

Material	**Electric conductivity**
Al_2O_3	10^{-14}
HfO_2	10^{-9}
TiO_2	10^{-7}

Thus, we can compute the electric field of each dielectric layer. Subsequently, we employ the obtained electric field to calculate the approximate spectral density of that layer, following a similar procedure as with our previous resonator. Since excess noise in a resonator is additive, we can infer that the sum of these three values can provide us with the approximate total STLS of our resonator.

$$S_{\mathrm{TLS(total)}} = S_{\mathrm{TLS1}} + S_{\mathrm{TLS2}} + S_{\mathrm{TLS3}} \tag{25}$$

Comparing the results presented in **Tables 1** and **4** reveal an approximately 30% decrease in S_{TLS} after incorporating two additional dielectric layers into the capacitor structures. Although these outcomes are approximate, we can confidently assert that this represents a significant improvement.

Table 4. Results of our improved LEKID with a three-layer dielectric between capacitor plates.

	Three layer dielectric
$\varepsilon_{\mathrm{effective}}$	28.33
C	$C1$ = 0.7692
	$C2$ = 1.9231
	$C3$ = 3.8462
	CT = 0.4808
R	$R1 = 1.3000 \times 10^{+15}$
	$R2 = 1.3000 \times 10^{+10}$
	$R3 = 1.3000 \times 10^{+8}$
	$RT \approx 1.3000 \times 10^{+15}$
E	$E1 = 5.7600 \times 10^{-9}$
	$E2 = 3.8400 \times 10^{-9}$
	$E3 = 1.9200 \times 10^{-9}$
S_{TLS}	$S_{\mathrm{TLS1}} = 5.7871 \times 10^{+21}$
	$S_{\mathrm{TLS2}} = 8.6806 \times 10^{+21}$
	$S_{\mathrm{TLS3}} = 1.7361 \times 10^{+22}$
	$S_{\mathrm{TLS(total)}} = 3.1829 \times 10^{+22}$

8. Conclusion

Gao's semi-empirical model for TLS noise offers insights into explaining TLS noise behavior in microwave kinetic inductance detectors (MKIDs). According to this model, the TLS power density in an LC resonator with a parallel plate capacitor primarily depends on factors such as electric field, electrical permittivity, and volume.

Therefore, by increasing these parameters, we can mitigate TLS noise. However, augmenting the electric field may induce nonlinearity in the resonator's performance. To address this, we proposed incorporating a three-layer dielectric between the capacitor plates, thereby simultaneously increasing permittivity and capacitor volume. Since the noise spectral density coefficient $\kappa(\nu, f_r, T)$ lacks a comprehensive theoretical explanation, exact values of S_{TLS}. could not be calculated. Instead, we employed simplified equations to derive approximate values for a parallel plate capacitor with a single layer of Al_2O_3. Subsequently, we developed a resonator based on the parallel plate capacitor, comprising three layers of Al_2O_3, HfO_2, and TiO_2 with equal thickness between the capacitor plates, to explore the impact on S_{TLS}. Our investigation revealed that by modifying the original structure, we could reduce S_{TLS} by up to 30%, representing a significant improvement.

Author contribution: Conceptualization, ZE and SMHJ; methodology, ZE and SMHJ; software, ZE, MBH; validation, ZE and SMHJ; formal analysis, ZE; investigation, ZE; resources, ZE; data curation, ZE; writing—original draft preparation, ZE; writing—review and editing, ZE; visualization, ZE and MBH; supervision, SMHJ; project administration, SMHJ; funding acquisition, None. All authors have read and agreed to the published version of the manuscript.

Conflict of interest: The authors declare no conflict of interest.

References

1. Mazin BA, Bailey J, Bartlett J, et al. Optical and Near-IR Microwave Kinetic Inductance Detectors (MKIDs) in the 2020s. Bulletin of the American Astronomical Society. 2019; 51(7).
2. Day PK, LeDuc HG, Mazin BA, et al. A broadband superconducting detector suitable for use in large arrays. Nature. 2003; 425(6960): 817-821. doi: 10.1038/nature02037.
3. D'Addabbo A, Bellini F, Cardani L, et al. High-sensitivity Kinetic Inductance Detectors for CALDER. arXiv. 2017; arXiv:1705.04483.
4. Miller JM, Zobrist N, Ulbricht G, et al. Improving the energy resolution of photon counting microwave kinetic inductance detectors using principal component analysis. Journal of Astronomical Telescopes, Instruments, and Systems. 2021; 7(04). doi: 10.1117/1.jatis.7.4.048003.
5. Vissers MR, Austermann JE, Malnou M, et al. Ultrastable millimeter-wave kinetic inductance detectors. Applied Physics Letters. 2020; 116(3). doi: 10.1063/1.5138122.
6. Mazin BA. Microwave Kinetic Inductance Detectors [PhD thesis]. California Institute of Technology; 2004.
7. Stevenson TR, Adams JS, Wen-Ting Hsieh, et al. Superconducting Films for Absorber-Coupled MKID Detectors for Sub-Millimeter and Far-Infrared Astronomy. IEEE Transactions on Applied Superconductivity. 2009; 19(3): 561-564. doi: 10.1109/tasc.2009.2019661
8. Shafiee M, Fedorov D, Grossan B, et al. A readout system for microwave kinetic inductance detectors using software defined radios. Journal of Instrumentation. 2021; 16(07): P07015. doi: 10.1088/1748-0221/16/07/p07015
9. Ishino H, Kibayashi A, Hattori K, et al. Development of Microwave Kinetic Inductance Detectors for a Detection of Phonons. Journal of Low Temperature Physics. 2013; 176(3-4): 161-167. doi: 10.1007/s10909-013-1025-0
10. Guruswamy T. Nonequilibrium behaviour and quasiparticle heating in thin film superconducting microwave resonators [PhD thesis]. University of Cambridge; 2018.
11. Ulbricht G, De Lucia M, Baldwin E. Applications for Microwave Kinetic Induction Detectors in Advanced Instrumentation. Applied Sciences. 2021; 11(6): 2671. doi: 10.3390/app11062671
12. Calvo M, Giordano C, Battiston R, et al. Development of Kinetic Inductance Detectors for Cosmic Microwave Background experiments. Experimental Astronomy. 2010; 28(2-3): 185-194. doi: 10.1007/s10686-010-9197-y

13. Ishitsuka H, Ikeno M, Oguri S, et al. Front-End Electronics for the Array Readout of a Microwave Kinetic Inductance Detector Towards Observation of Cosmic Microwave Background Polarization. Journal of Low Temperature Physics. 2016; 184(1-2): 424-430. doi: 10.1007/s10909-015-1467-7
14. Dober B, Austermann JA, Beall JA, et al. Optical Demonstration of THz, Dual-Polarization Sensitive Microwave Kinetic Inductance Detectors. Journal of Low Temperature Physics. 2015; 184(1-2): 173-179. doi: 10.1007/s10909-015-1434-3
15. Hu J, Salatino M, Traini A, et al. Proximity-Coupled Al/Au Bilayer Kinetic Inductance Detectors. Journal of Low Temperature Physics. 2020; 199(1-2): 355-361. doi: 10.1007/s10909-019-02313-4
16. Gao J, Mazin B, Daal M, et al. Power dependence of phase noise in microwave kinetic inductance detectors. SPIE Proceedings. 2006; 6275(1).
17. Gao J. The Physics of Superconducting Microwave Resonators [PhD thesis]. California Institute of Technology; 2008.
18. Noroozian O. Superconducting microwave resonator arrays for submillimeter/far-infrared imaging [PhD thesis]. California Institute of Technology; 2012.
19. Zobrist N, Daal M, Corbin JY, et al. Disk Resonator Design for Kinetic Inductance Detectors. Journal of Low Temperature Physics. 2018; 194(5-6): 394-403. doi: 10.1007/s10909-018-02125-y
20. Baselmans J. Kinetic Inductance Detectors. Journal of Low Temperature Physics. 2012; 167(3-4): 292-304. doi: 10.1007/s10909-011-0448-8
21. Doyle S, Mauskopf P, Naylon J, et al. Lumped Element Kinetic Inductance Detectors. Journal of Low Temperature Physics. 2008; 151(1-2): 530-536. doi: 10.1007/s10909-007-9685-2
22. Doyle S, Mauskopf P, Zhang J, et al. Optimisation of Lumped Element Kinetic Inductance Detectors for use in ground based mm and sub-mm arrays. AIP Conference Proceedings. 2009; 1185(1).
23. Verheul S. Ultra High Kinetic Inductance Detectors [Master's thesis]. Delft University of Technology; 2019.
24. De Lucia M, Ulbricht G, Baldwin E, et al. Limitations to the energy resolution of single-photon sensitive microwave kinetic inductance detectors. AIP Advances. 2023; 13(12). doi: 10.1063/5.0168365
25. Cardani L, Colantoni I, Cruciani A, et al. Energy resolution and efficiency of phonon-mediated kinetic inductance detectors for light detection. Applied Physics Letters. 2015; 107(9). doi: 10.1063/1.4929977
26. Schlaerth J, Golwala S, Zmuidzinas J, et al. Sensitivity Optimization of Millimeter/Submillimeter MKID Camera Pixel Device Design. AIP Conference Proceedings. 2009; 1185(1).
27. Leduc HG, Bumble B, Day PK, et al. Titanium nitride films for ultrasensitive microresonator detectors. Applied Physics Letters. 2010; 97(10). doi: 10.1063/1.3480420
28. Mazin BA, Day PK, Zmuidzinas J, Leduc HG. Multiplexable kinetic inductance detectors. AIP Conference Proceedings. 2002; 605(1).
29. Baselmans J, Barends R, Hovenier JN, et al. High Q Niobium superconducting resonators for use as Kinetic Inductance sensing elements Proceedings of the European Interferometry Initiative Workshop organized in the context of the 20005 Joint European and National Astronomy Meeting "Distant Worlds". Bulletin de la Société Royale des Sciences de Liège. 2005; 74(5-6): 491-497.
30. Doyle S, Dunscombe C, Mauskopf P, et al. Detection of Terahertz radiation using large Niobium detector arrays. In: Proceedings of the 16th International Symposium on Space Terahertz Technology.
31. Mazin BA, Bumble B, Day PK, et al. Position sensitive x-ray spectrophotometer using microwave kinetic inductance detectors. Applied Physics Letters. 2006; 89(22). doi: 10.1063/1.2390664
32. Barends R, Baselmans JJA, Hovenier JN, et al. Niobium and Tantalum High Q Resonators for Photon Detectors. IEEE Transactions on Applied Superconductivity. 2007; 17(2): 263-266. doi: 10.1109/tasc.2007.898541
33. Baselmans J, Yates SJC, Barends R, et al. Noise and Sensitivity of Aluminum Kinetic Inductance Detectors for Sub-mm Astronomy. Journal of Low Temperature Physics. 2008; 151(1-2): 524-529. doi: 10.1007/s10909-007-9684-3
34. Kumar S, Gao J, Zmuidzinas J, et al. Temperature dependence of the frequency and noise of superconducting coplanar waveguide resonators. Applied Physics Letters. 2008; 92(12).
35. Gao J, Daal M, Martinis JM, et al. A semiempirical model for two-level system noise in superconducting microresonators. Applied Physics Letters. 2008; 92(21). doi: 10.1063/1.2937855
36. Noroozian O, Gao J, Zmuidzinas J, et al. Two-level system noise reduction for Microwave Kinetic Inductance Detectors. AIP Conference Proceedings. 2009; 1185(1).
37. Czakon NG, Schlaerth JA, Day PK, et al. Optimization of MKID noise performance via readout technique for astronomical

applications. SPIE Proceedings. 2010; 7441.
38. Yates SJC, Baselmans JJA, Endo A, et al. Photon noise limited radiation detection with lens-antenna coupled microwave kinetic inductance detectors. Applied Physics Letters. 2011; 99(7): 073505. doi: 10.1063/1.3624846
39. Shirokoff E, Barry PS, Bradford CM, et al. MKID development for SuperSpec: An on-chip, mm-wave, filter-bank spectrometer. SPIE Proceedings. 2012; 8452(1).
40. Janssen RMJ, Baselmans JJA, Endo A, et al. High optical efficiency and photon noise limited sensitivity of microwave kinetic inductance detectors using phase readout. Applied Physics Letters. 2013; 103(20): 203503. doi: 10.1063/1.4829657
41. Lowitz AE, Brown AD, Stevenson TR, et al. Design, fabrication, and testing of lumped element kinetic inductance detectors for 3 mm CMB Observations. SPIE Proceedings. 2014; 9153(1)
42. Araujo DC, Ade PAR, Bond JR, et al. A LEKID-based CMB instrument design for large-scale observations in Greenland. SPIE Proceedings. 2014; 9153(1).
43. Ji C. Design of antenna-coupled lumped-element titanium nitride KIDs for long-wavelength multi-band continuum imaging. California Institute of Technology; 2015.
44. McCarrick H, Abitbol MH, Ade PAR, et al. Development of dual-polarization LEKIDs for CMB observations. SPIE Proceedings. 2016; 9914(1).
45. Johnson BR, Flanigan D, Abitbol MH, et al. Polarization sensitive Multi-Chroic MKIDs. SPIE Proceedings. 2016; 9914(1).
46. Bueno J, Yurduseven O, Yates SJC, et al. Full characterisation of a background limited antenna coupled KID over an octave of bandwidth for THz radiation. Applied Physics Letters. 2017; 110(23). doi: 10.1063/1.4985060
47. Beldi S, Boussaha F, Hu J, et al. High Q-factor near infrared and visible Al2O3-based parallel-plate capacitor kinetic inductance detectors. Optics Express. 2019; 27(9): 13319. doi: 10.1364/oe.27.013319
48. Hornsby AL, Barry PS, Doyle SM, et al. Reducing the Susceptibility of Lumped-Element KIDs to Two-Level System Effects. Journal of Low Temperature Physics. 2020; 200(5-6): 239-246. doi: 10.1007/s10909-020-02501-7
49. Hailey-Dunsheath S, Janssen RMJ, Glenn J, et al. Kinetic inductance detectors for the Origins Space Telescope. Journal of Astronomical Telescopes, Instruments, and Systems. 2021; 7(01). doi: 10.1117/1.jatis.7.1.011015
50. Sueno Y, Honda S, Kutsuma H, et al. Characterization of two-level system noise for a microwave kinetic inductance detector comprising niobium film on a silicon substrate. Progress of Theoretical and Experimental Physics. 2022; 2022(3). doi: 10.1093/ptep/ptac023
51. Hood JC, Barry PS, Cecil T, et al. Testing Low-Loss Microstrip Materials with MKIDs for Microwave Applications. Journal of Low Temperature Physics. 2022; 209(5-6): 1189-1195. doi: 10.1007/s10909-022-02881-y
52. Pan Z, Dibert KR, Zhang J, et al. Noise Optimization for MKIDs With Different Design Geometries and Material Selections. IEEE Transactions on Applied Superconductivity. 2023; 33(5): 1-8. doi: 10.1109/tasc.2023.3250167